Electronic supplementary information for

Dramatically enhanced reversibility of Li_2O in SnO_2-based electrodes: the effect of nanostructure on high initial reversible capacity

Renzong Hu,[a, b] Dongchang Chen,[b] Gordon Waller,[b] Yunpeng Ouyang,[a] Yu Chen,[b] Bote Zhao,[b] Ben Rainwater,[b] ChenghaoYang,[c] Min Zhu,*[a] Meilin Liu*[b, c]

[a] School of Materials Science and Engineering, South China University of Technology, Guangzhou, 510640, China. E-mail: memzhu@scut.edu.cn

[b] School of Materials Science and Engineering, Georgia Institute of Technology, Atlanta, GA 30332-0245, USA. E-mail: meilin.liu@mse.gatech.edu

[c] School of Environment and Energy, South China University of Technology, Guangzhou, 510006, China

This document includes

Supplementary figures (**Fig.S1-15**) and Table (**Table S1**)

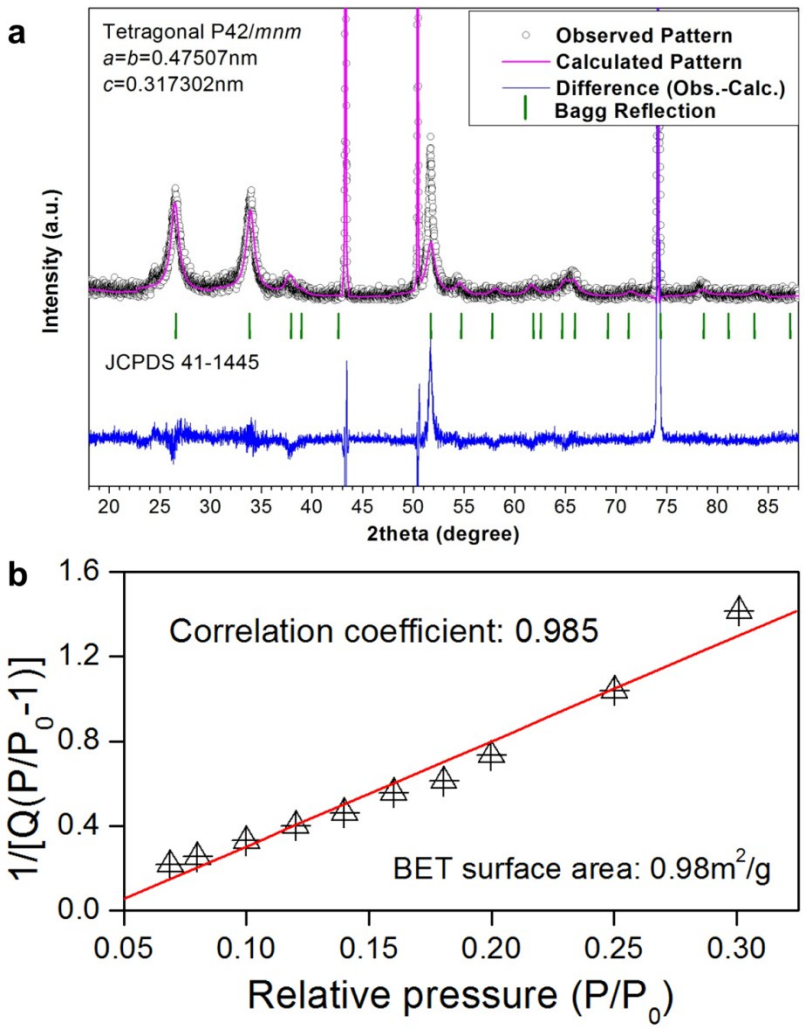

Fig.S1 (a) Rietveld refinement XRD for the as-sputtered SnO_2 film. Except those peaks of Cu substrate, all peaks were indexed to single-phase tetragonal (P42/mnm) SnO_2. From all peaks, crystallite size for SnO_2 is estimated to be 9.45nm, and no microstrain broadening was determined by the fitting, which are in good agreement with Scherer Equation estimation of crystallite size using FWHM of peaks at 26.5° and 33.9° with an average value of 8.85nm. The SnO_2 lattice is nominally tetragonal with a=b=0.4736nm and c=0.3187nm (JCPDS 41-1445). Rietveld refinement of unit cell shows a small compression of the *c* axis and elongation of the *a/b* to *a*=*b*=0.47507nm and *c*=0.317302nm. Furthermore, a small amount of preferred orientation along *c*-axis to form plates is also observed. (**b**) BET specific surface area of the SnO_2 thin film by N_2absorption, indicating a very small surface area of 0.98m^2/g for the SnO_2 layer.

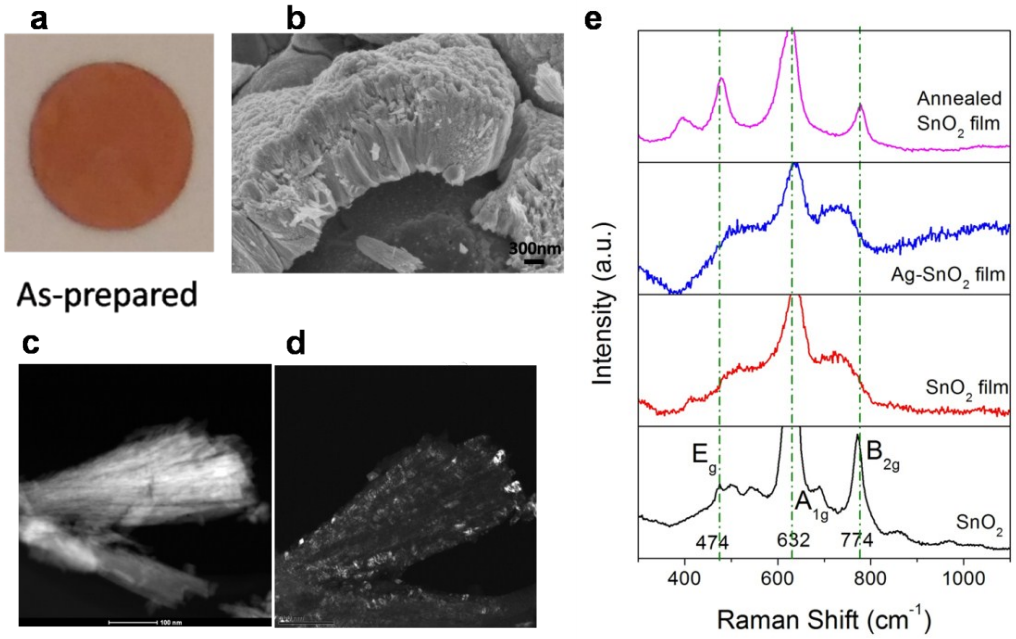

Fig.S2 (**a**) Optical images for the as prepared SnO_2 film, showing the colourless transparent SnO_2 layer.(**b**) SEM image for the cross-section of the SnO_2 layer, showing its columnar structure with a thickess of around 900nm;(**c** and **d**) STEM and dark-field TEM image for a small bundle of SnO_2 scrapped off the Cu substrate, revealing its nano-columnar strucuture and the homogeneous distribution of SnO_2 nanocrystals inside the SnO_2bundle. **(e)** Raman data for the SnO_2 film after different treatment in comparison with that of a commercial SnO_2 powder (99% purity, particle size~10μm). Obvious A_{1g}, B_{2g}, E_g bands of SnO_2phase can be found in the as-prepared and Ag-coated SnO_2 film. However, the E_g band undergoes a blue shift while the B_{2g} band undergoes a red shift, presumably due to the nano-effects, inner-stress during film growth, and/or the preferred orientation of SnO_2nanocrystals, because both of them matched well with those of the powder after annealing the film in Ar at 500°C for 4hours. Furthermore, another detectable peak at around 395cm^{-1} is present in the annealed SnO_2 film, which could be attributed to structural transformation of the SnO_2 during film annealing. Several peaks at low wave-number portion from 350 to 420 cm^{-1} were also frequently found in the nanocrystalline-amorphous SnO_2 films (ref.25), and Ag-coated SnO_2 bulk materials(ref.27) due to the multiple optical normal modes of vibrations in SnO_2 lattice. We found that Ag nanoparticles coated on the surface of SnO_2does not induce obvious change in Raman spectrum. The Ag-coating SnO_2 sample was used for *in*-situ SERS studies.

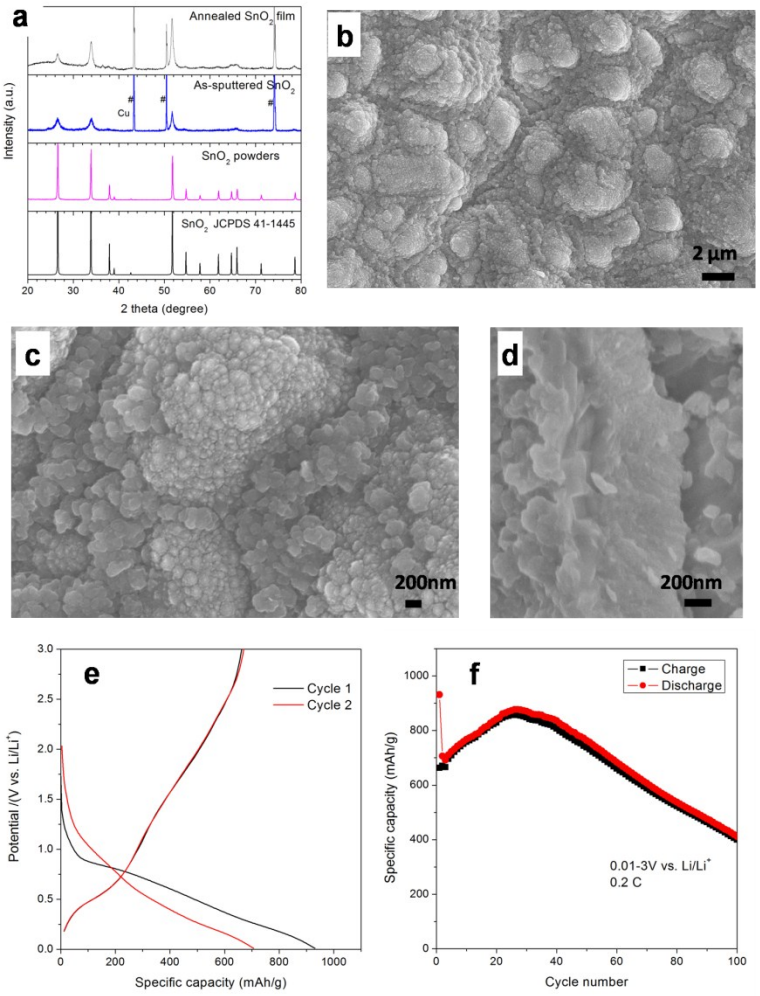

Fig. S3 (a) XRD patterns of the SnO_2 powder, as-sputtered SnO_2 film, and the film after annealing, indicating that all the visible diffraction peaks in these three samples meet well the tetragonal SnO_2 (JCPDS 41-1445). SEM images for top-view **(b, c)** and cross-section **(d)** of the SnO_2 layer after annealing. **(e)** Capacity-potential curves for the first and second cycles, and (f) cycle performance of the annealed SnO_2 film with thickness of 0.9μm.It could be seen that the morphology of the film had been dramatically changed after annealing in Ar at 500°C for 4h. The voids among the macro/micro-columns found in the as-prepared sample have collapsed as the nanosized SnO_2 grains fused to form a dense film. The cross-section image also reveals that as a result of annealing the SnO_2 film layer lost the columnar structure and the boundaries among the nano-columns. Consequently, the annealed film has a much lower initial Coulombic efficiency (70.9%) and inferior capacity retention (60% of the first reversible capacity after 100 cycles) than the film without annealing. These findings help support our original claim that the columnar and porous SnO_2 film morphology is critical for good electrochemical reversibility.

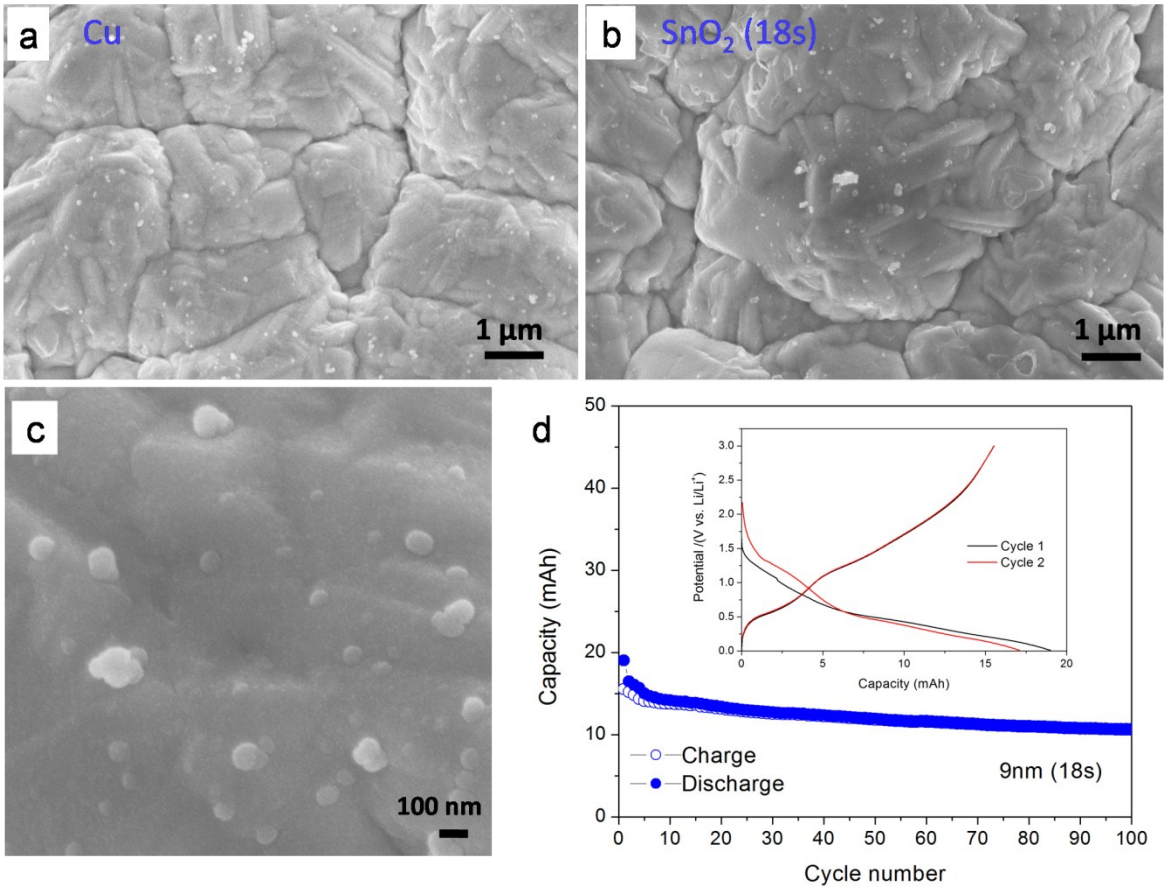

Fig.S4 SEM images for surface morphology of SnO_2 film sputtered at different time. **(a)** 0 second; **(b)** 18seconds； **(c)** Magnified SEM image for the surface morphology of film in (b); **(d)** The first two capacity- potential curves and cycle performance of the 9nm SnO_2 films. It can be seen that the morphology of the film was dramatically affected by the morphology of Cu substrate because the SnO_2 layer is too thin. The magnified SEM images show that the film does not present similar microstructure with the 0.9μm film, which is lack of the nano-, micro, and macro-column structure and the multi-scale boundary distributions. These also lead to a dense SnO_2 layer in the thin film. And thus, it yielded quite different electrochemical properties. As we could not determine the accurate mass of SnO_2 in the 9nm thin film, capacity (mAh) rather than specific capacity (mAh/g) was given. The initial Coulombic efficiency of the 9nm film is 81.7%, with capacity retention of 68.6% after 100 cycles, which are inferior to those of the 0.9um film. This suggests that the unique microstructure, in particular the multi-scale column structure and the boundary distributions, is responsible for the enhanced performance of the 0.9um film.

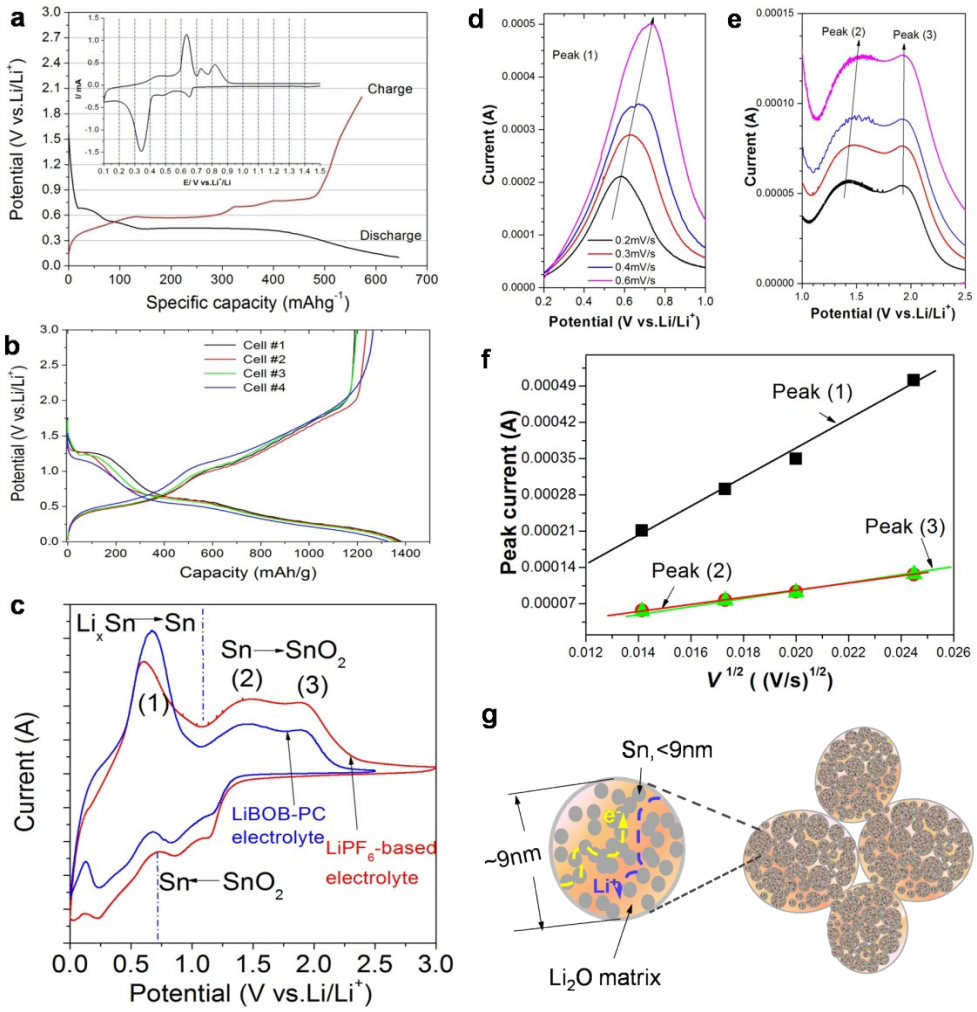

Fig.S5 (**a**) Discharge-charge curve and CV curve(inset) of pure Sn thin film, indicating that the lithium storage capacity in Sn mainly comes from the alloying-dealloying reactions at potential below 1.0V vs.Li/Li$^+$. (**b**) The1stdischarge-charge curves for four half cells with working electrode used the same SnO_2 film sample. The slight difference on discharge and charge curves, as well as capacity and ICE among these cells could be attributed to the heterogeneous structure in sputtered film. The error in weighing of the punched electrodes and the manual-assembly of the cells could also lead to some variation in the normalized capacities of the electrodes. (**c**) Comparison the CV curves of SnO_2 film electrode in different electrolytes with different salts and solvents, i.e. $LiPF_6$ in EC+DEC+FEC, and LiBOB in PC. It can be seen that in both electrolytes, the SnO_2 film electrodes present similar lithiation/delithiation behavior and reversibility. (**d** and **e**) CV curves of the SnO_2 film electrode measured with different scanning rates, 0.2,0.3,0.4, and 0.6mV/s, and (**f**) the relationship between I_p and $v^{1/2}$ for peak (1), (2) , (3) indicated in (A).Peak (1) is attributed to de-alloying of Li_xSn, while peaks (2) and (3) are related to reversing Li_2O and Sn to SnO_2. It can be seen that when the scanning rate v increases, the oxidation peaks shift slightly to higher potential with an increase in the peak height. A linear relationship exist between the oxidation peak current of all three peaks and the root of the scan

rate ($v^{1/2}$),indicates that the reaction kinetics is controlled by the Li^+ diffusion step. (**g**) Schematic of the electron and Li^+ conduction pathways in the lithiated SnO_2 electrodes. The Sn and Li_xSn nanoparticles would form connected networks in the Li_2O matrix. The Sn/Li_xSn networks serve as conductive paths for electrons, while the Li_2O provides a similar path for Li^+. The high fraction of Sn/Li_2O interface could enhance the kinetics of Li^+ migration in the Li_2O matrix.

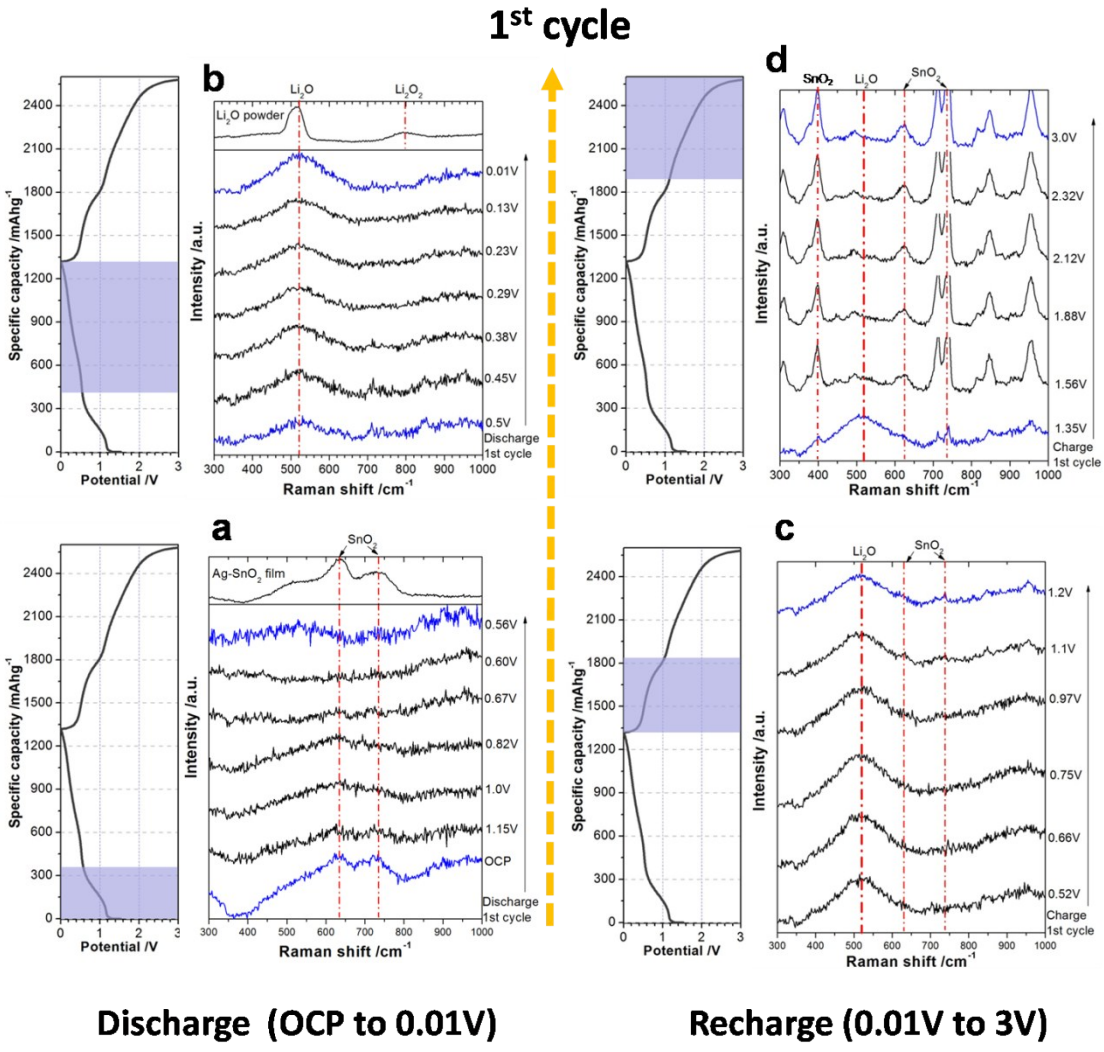

Fig.S6 *In situ* SERS data for potential (capacity)-lapsed structural evolution of the SnO_2 film electrode during the 1st discharge-charge cycle. (**a** and **b**) Discharge from OCP to 0.01V; (**c** and **d**) recharge from 0.01V to 3.0V. The *in situ* SERS data clearly presents the disappearance of SnO_2 and its regeneration along with direct evidence for the formation and decomposition of Li_2O during discharge and charge by observing the peak at ~520cm^{-1}.The weaker intensity at the OCV state in the first cycle was because excess electrolyte was covering the surface of SnO_2, which will decrease the effective laser intensity illuminating the surface of SnO_2. During cycling, the electrolyte would permeate the entire cell more comprehensively, which will decrease the thickness of electrolyte layers above the surface of SnO_2. Therefore, the effective laser power will be increased as cell cycles, leading to increased signal intensity of SnO_2 in the second cycle. Also, it is noted that at the end of charge, the regenerated SnO_2 present narrower band widths in the Raman spectrum. This could be due to that, in some zones, the regenerated nanosizeSnO_2 has a good crystalline and is free of stress and orientation structure.

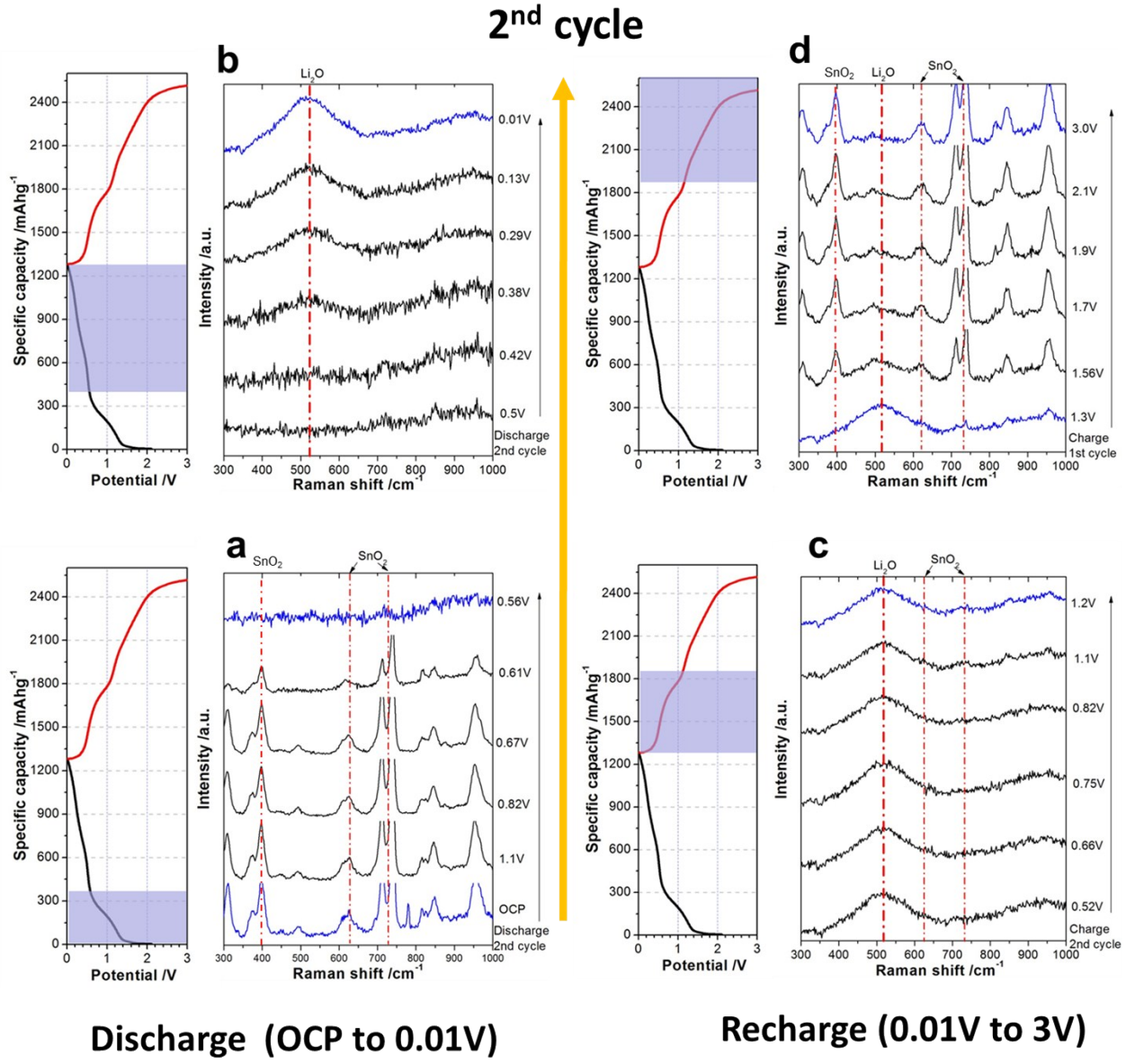

Fig.S7 *In situ* SERS data for potential (capacity)-lapsed structural evolution of the SnO_2 film electrode during the 2nd discharge-charge cycle. (**a** and **b**) Discharge from OCP to 0.01V; (**c** and **d**) recharge from 0.01V to 3.0V.

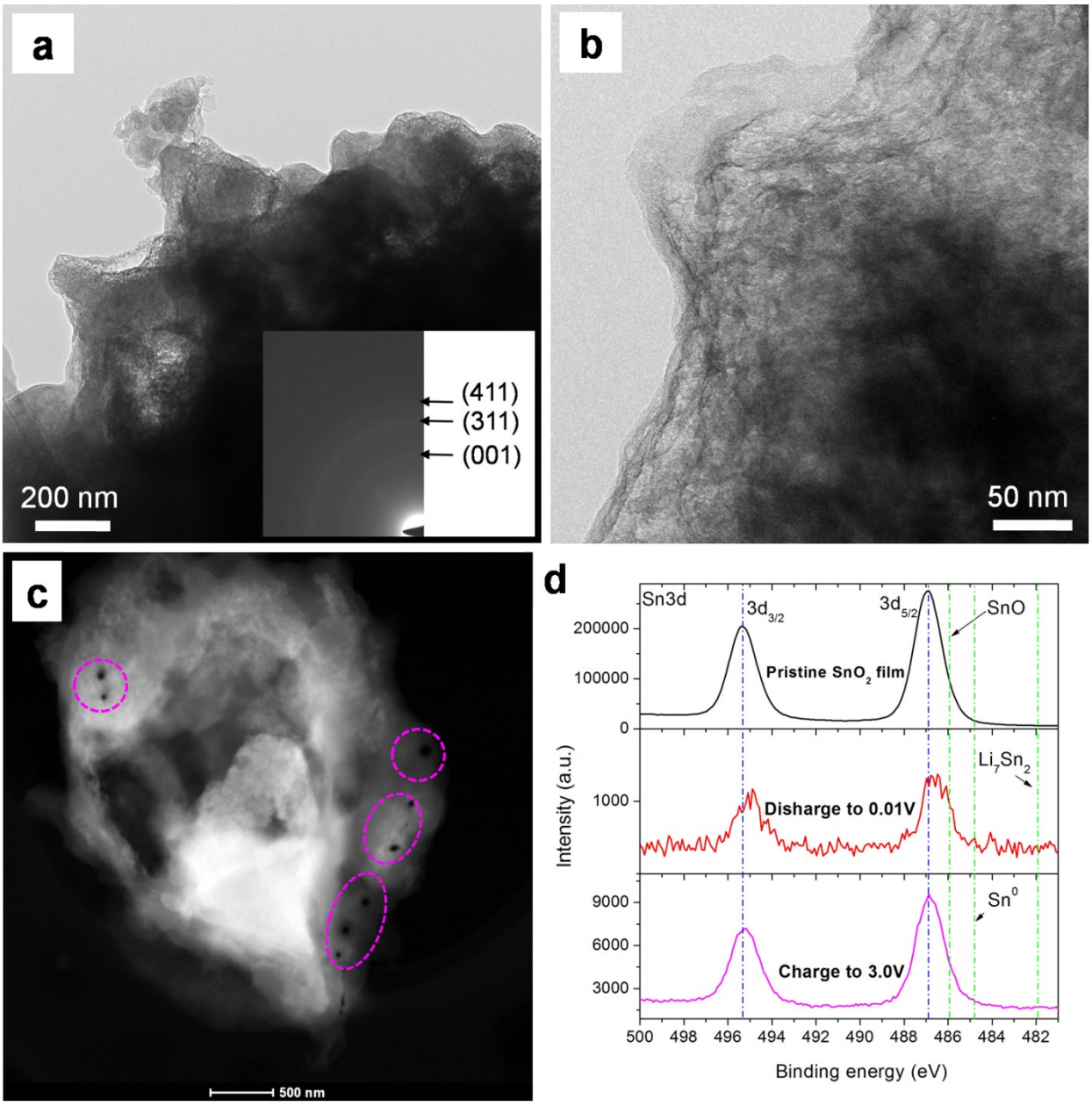

Fig.S8 Microstructure analysis of the SnO_2 film after first discharged to 0.01V. (**a**) Low magnification TEM image and SAED (inset), (**b**) high magnification TEM image, and (**c**) STEM of the SnO_2 film after discharge to 0.01V in the first cycle. The fully lithiated SnO_2 film electrode is unstable even at short exposure of electron beam in TEM. The morphology of the mixture tends to change fast during the exposure to electron beam due to the presence of ultrafine Sn and Li_xSn phase with low melting point. There are small holes (dotted circles) appeared in zones focused with electron beam during EELS collection. (**d**) XPS spectra for the Sn 3d levels at various depths of charge-discharge state (pristine, first discharge to 0.01 V (vs. Li/Li^+), first charge to 3.0V for the SnO_2 film electrodes. In the pristine SnO_2 film, the two strong peaks at ~486.9 and ~495.2 eV, are assigned to Sn $3d_{5/2}$and $3d_{3/2}$respectively. After the

film is discharged to 0.01V, these two peaks become much weaker due to the reduction of SnO_2. In addition, they shifted by about 0.5eV toward lower binding energies. This shift could be explained by the formation of the Li_xSn alloy according to reference. However, the XPS signal of the Li_xSn phase was not very strong at the fully lithiated SnO_2, which might be attributed to the embedded Li_xSn in the amorphous Li_2O matrix and the coverage of the SEI layer. In addition, as the fully lithiated SnO_2 sample is highly sensitive to air, thus the Li_xSn and Sn could be quickly oxidized to formed thin SnO_2 layer on the near surface during the film transfer from the Ar-filled glove box to the XPS. Nevertheless, the characteristic XPS peaks for SnO_2became stronger after the electrode is recharged to 3.0 V (vs. Li/Li^+), with the same binding energies for Sn $3d_{5/2}$ and $3d_{3/2}$ as in the as-sputtered film. Fitting of the Sn $3d^{5/2}$ XPS also suggested that the SnO_2 is the dominant phase in the charged film. These confirm that the matrix Li_2O could react with newly formed metallic Sn to yield SnO_2 during charge. This is in agreement with the *ex situ* XRD and the *in situ* SERS results.

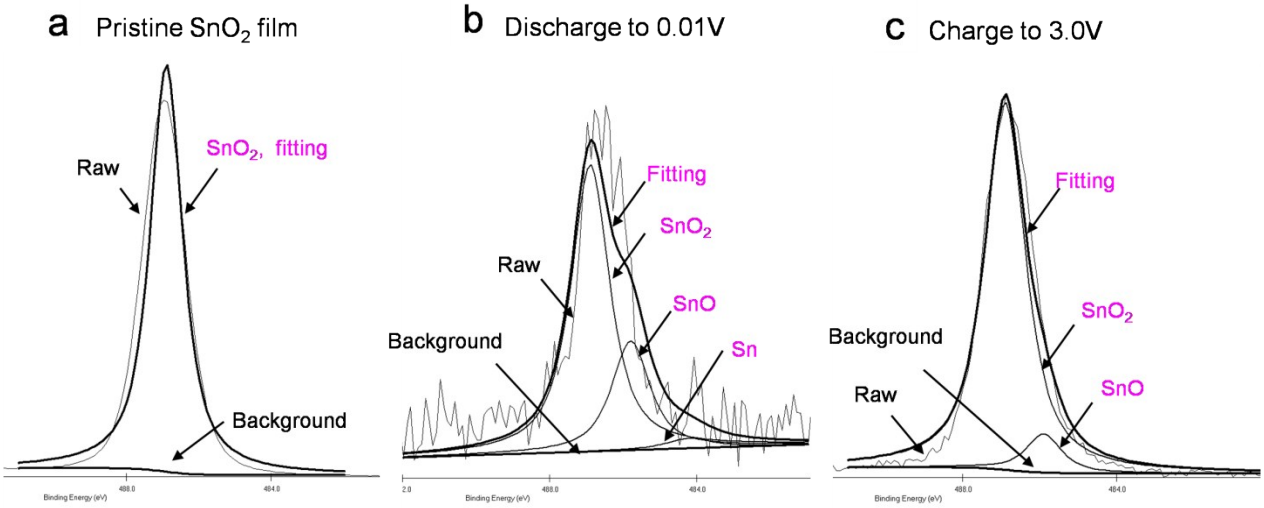

Fig.S9 Fitting of the Sn $3d^{5/2}$ XPS of the SnO_2 film at different depths of charge- discharge state: (a) pristine, (b) first discharged to 0.01 V (vs. Li/Li^+), (c) first charged to 3.0V (vs. Li/Li^+), suggesting that the SnO_2 is the dominant phase in the charged film.

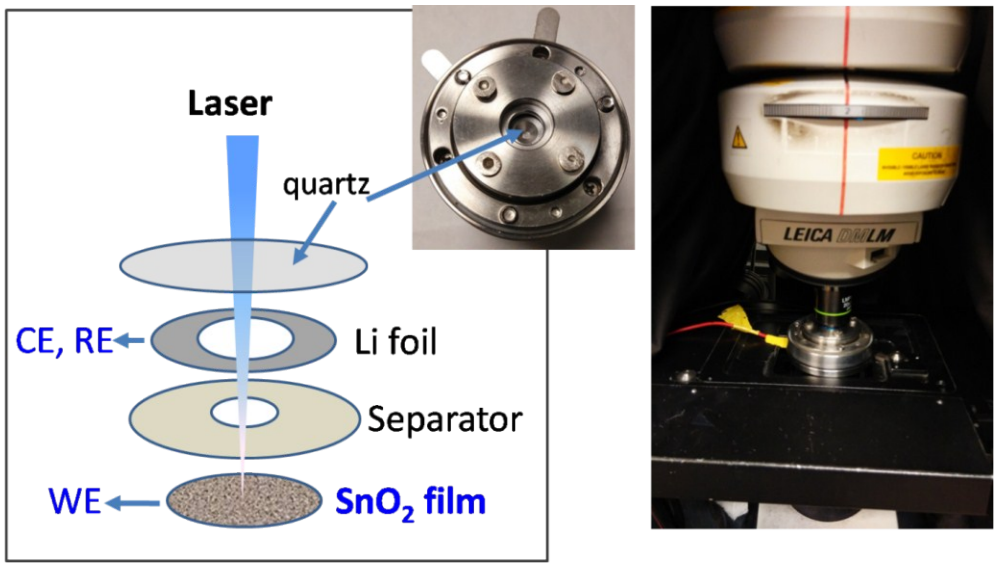

Fig.S10 Schematic drawing, optical images showing the spectroelectrochemical cell configuration and operation for in-situ SERS testing. The cells, with liqiud state electrolyte of LiBOB in PC, were assembled in Ar-filled glovebox.

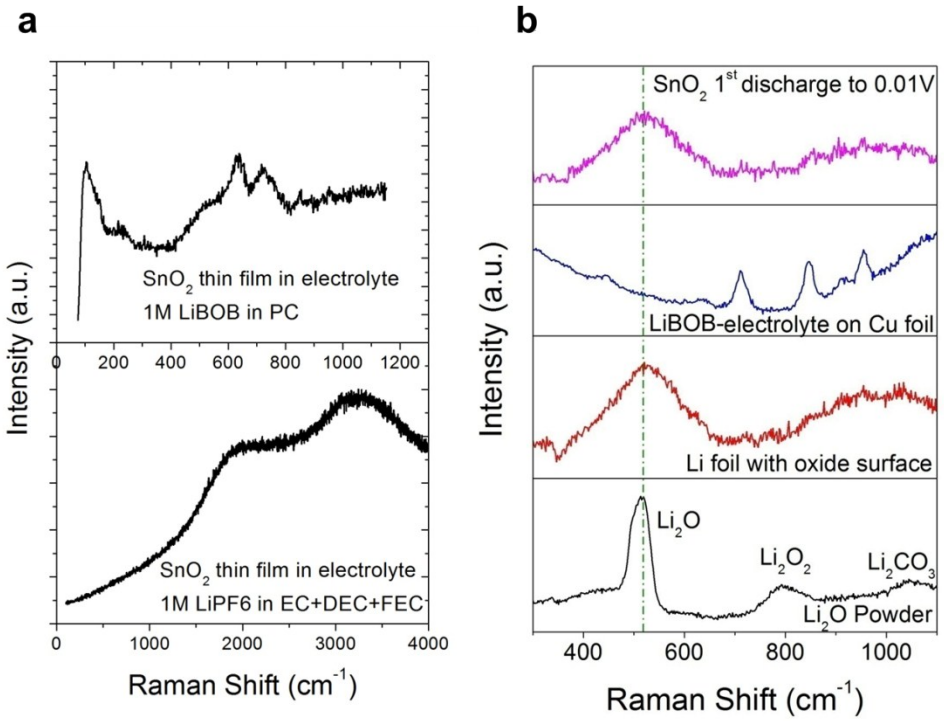

Fig.S11 (**a**) Comparison of the Raman spectrum of SnO_2 thin film in $LiPF_6$ based electrolyte and LiBOB-based electrolyte, showing that there was serious fluorescence effect in case of $LiPF_6$ based electrolyte, which covered all the signals of SnO_2. The Raman spectrum at OCP shows lower peak intensity for SnO_2 due to the covering of electrolyte and Ag nanoparticles on the film surface. (**b**) Raman data from the SnO_2 film electrode at the end of 1stdischarge to 0.01V in 1M LiBOB–PC showing obvious Li_2O formation, which has similar spectrum to that collected for the oxide surface of Li foil. Previous reports indicate that Li_2O is not evident in *insitu* XRD, or *insitu* TEM due to its poor crystallinity in the lithiated SnO_2 electrode. In addition, Li_2O is sensitive to air and moisture, thus it is necessary to use techniques such as *insitu* SERS to observe its formation and decomposition in electrochemical cells. The Raman spectrum of LiBOB also has three detectable peaks, however at different regions of the Raman spectrum in comparison with those of SnO_2 and Li_2O.

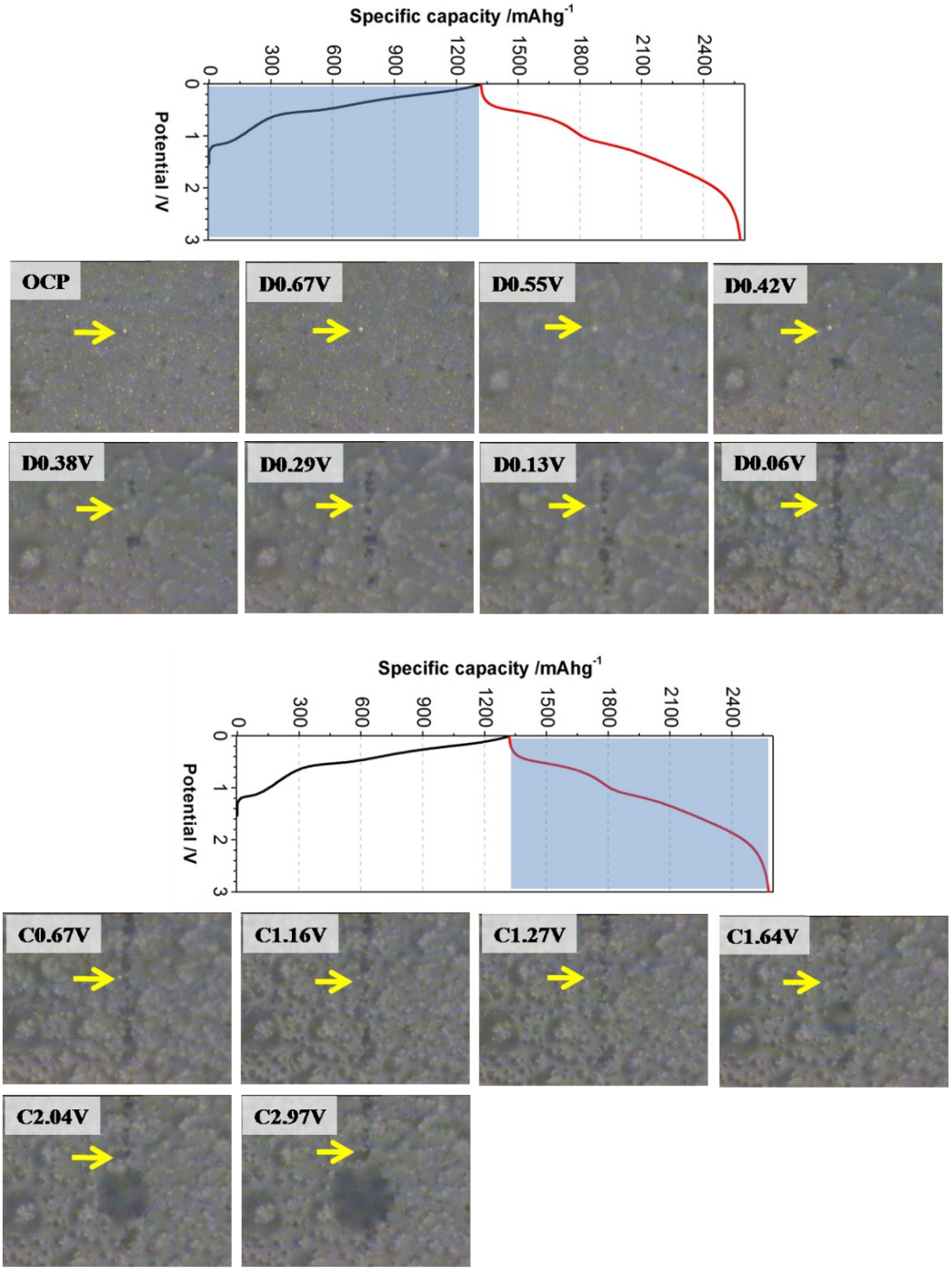

Fig.S12 Optical images for the SnO_2 film electrode at different potential states during the 1st discharge-charge cycle. They were recorded by the CCD camera coupled with the Raman systemduring collectiion of the *insitu* SERS data, showing the volume variation and surface mophology change of the film during Li^+ insertion and extraction.

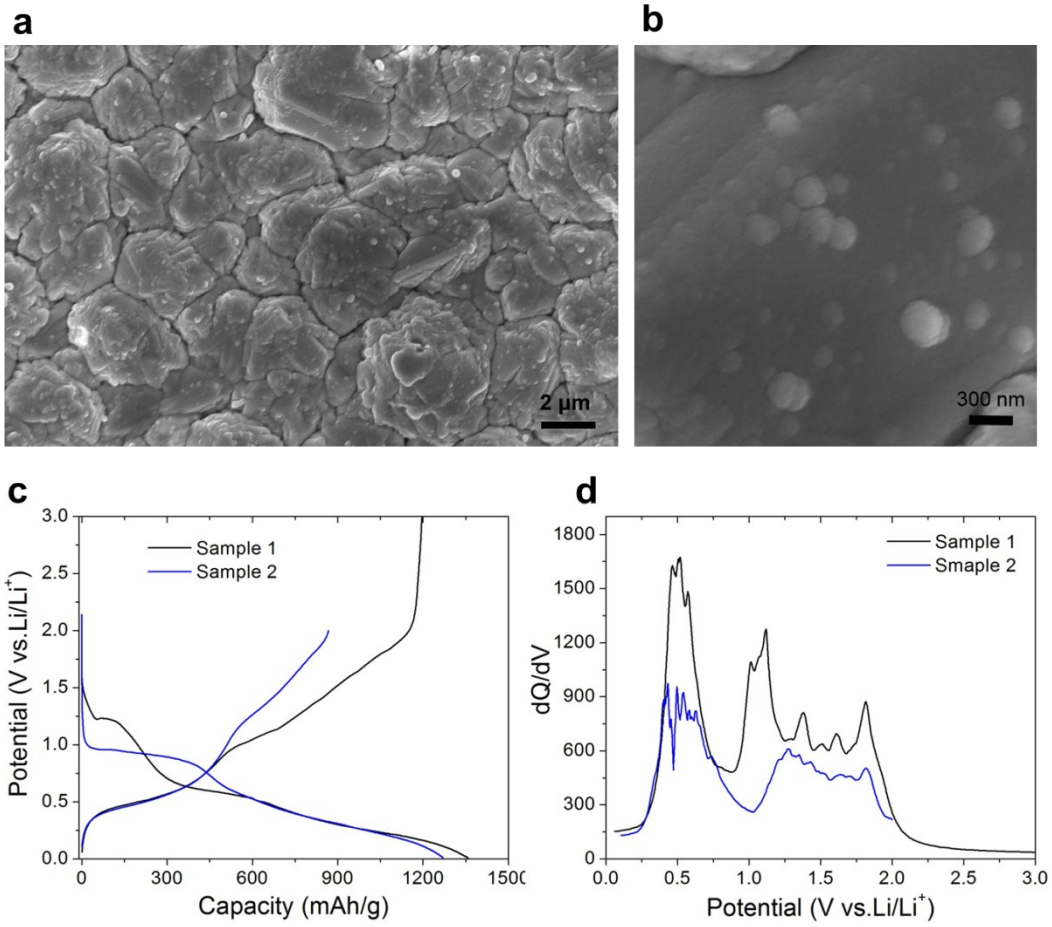

Fig .S13 SEM image (**a**) and enlarged SEM image(**b**) of another sputtered SnO_2 film (sample 2),using the same power(150W, 30min) and working gas pressure(2.0Pa)as those for sample 1 which was discussed in detail for this work, however sample 2 was produced with continuous rotation for the Cu substrate during sputtering. It can be found that sample 2 is much denser and without the obvious three structural units: nano-, micro-, and macro-columns, together with associated nano-, micro, and macro-void distributions; (**c** and **d**) comparison of the 1stdischarge-charge curves, differential charge capacities for the two SnO_2 film samples, indicating that the sample 1 presents much better reversibility of lithiation /delithiation and thus much higher ICE.

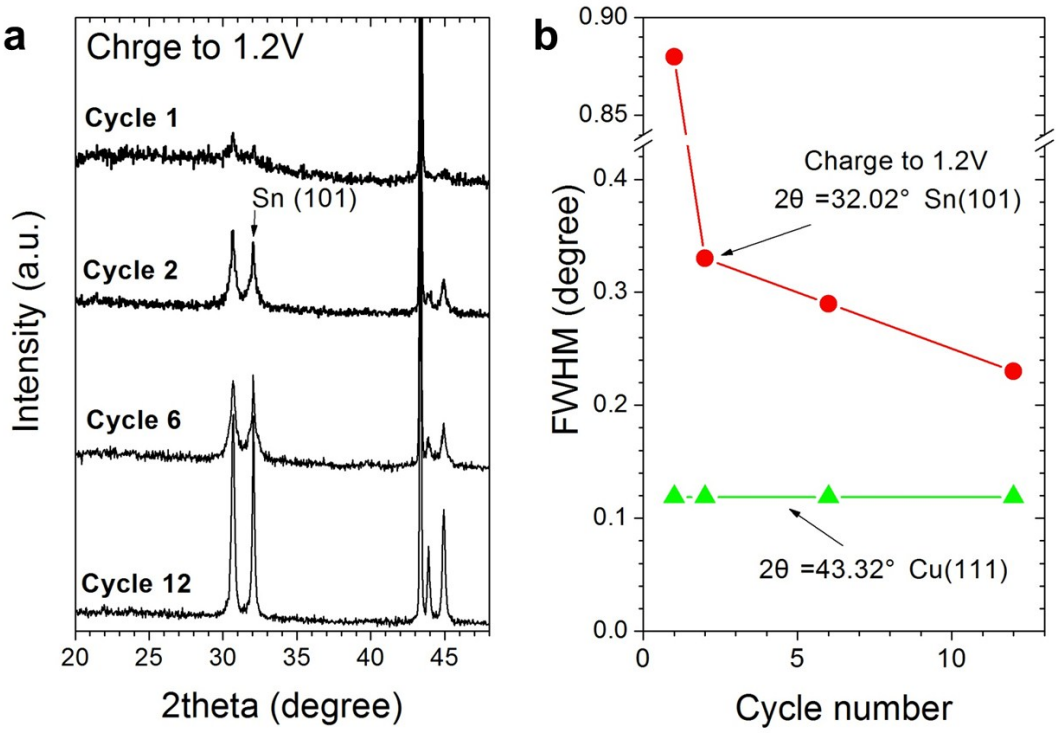

Fig .S14 (**a**) Comparison of *exsitu* XRD partterns for the SnO_2 electrode recharged to 1.2V after different cycle numbers(1^{st}, 2^{nd}, 6^{th}, 12^{th}); (**b**) The full width at half maximum(FWHM) for Sn (101) diffraction peak *vs.* cycle number. The gradually decrease of FWHM indicates the coarsening of Sn crystals during cycling.

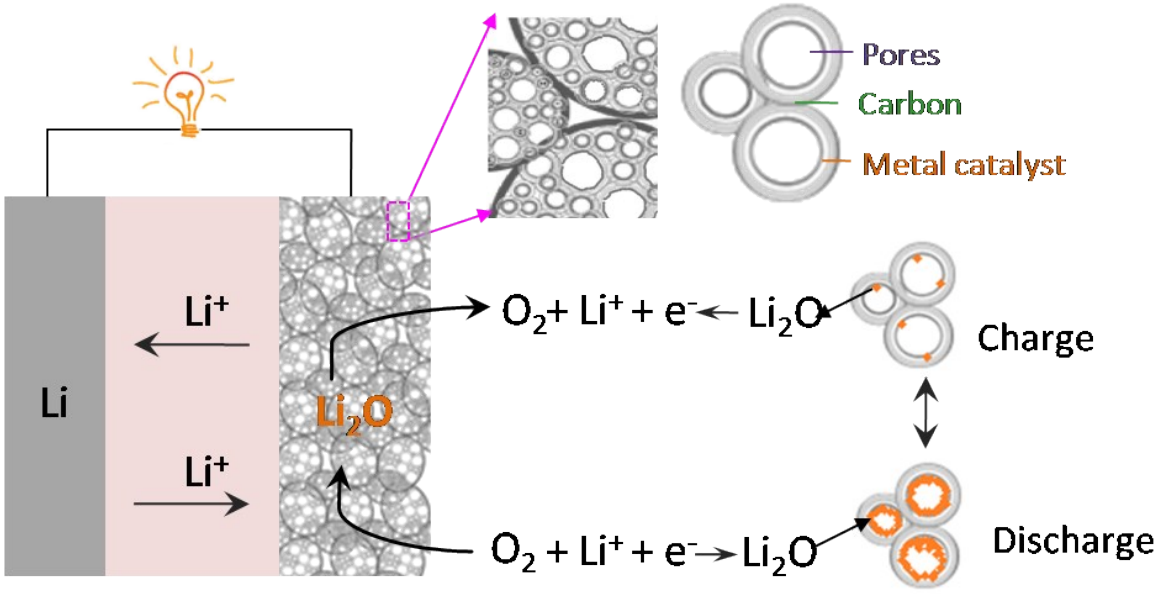

Fig.S15 Schematic diagram for a Li-O_2 battery.The cathode is designed to have a hierarchical construction for porous carbon and its loading metal and/or oxides catalysts, where the catalysts mainly disperse on the inner surfaces of multi-scale carbon pores rather than inside the carbon frameworks. During discharge, O_2 react with Li^+ in pores to form Li_2O mainly on the surfaces of catalyst. Due to direct contact with the well selected catalyst and the Li_2O phase formed during discharge, the decomposition of Li_2O could be complete at modest potential ranges during charge. This hierarchical structure is expected to maintain fast transport of O_2 and good contact between Li^+, Li_2O and catalysts in O_2cathode during Li-O_2 battery operation.

Table S1 Diffusion coefficient of Li^+ in different kinds of lithiated SnO_2 materials

Reaction /materials	D_{Li+} **(m^2/s)**	**References**
(peak 1) $Li_xSn—Li^+ +Sn$	1×10^{-11}	This work
(peak 2, 3) $Li_2O+Sn—Li^+ +SnO_2$	6×10^{-13}	This work
Li_2O in lithiatedSnO_2 single nanowire	5×10^{-16}~5×10^{-14}	Ref.14
lithiated amorphous SnO_2 thin film	10^{-15}~10^{-13}	Ref. 23

Based on the CV results shown in Fig.S5, we can determine the diffusivity of Li^+ during the reaction by the following equation,

$I_p=2.69\times10^5An^{3/2}C_0D^{1/2}v^{1/2}$

Where n is the number of electrons per molecules during the intercalation (Li^+, n=1), A is the surface area of the electrode (0.317cm^2 in this work), C_0 is the initial concentration of lithium ions (1mol/L in electrolyte). D is the diffusion coefficient of Li^+. On the basis of our data, the D_{Li+} in different reactions were calculated and listed in **Table S1** below, compared with that of in other lithiated SnO_2 materials.

The diffusion distance (l) of Li^+ during the time (at 1/5C rate) for reverse reaction of Li_2O to SnO_2, i.e. decomposition of SnO_2 among potential range of 1.0-3.0V (take about 8000s), was approximately evaluated by the following equation:

$l=\sqrt{Dt}$

Accordingly, a diffusion distance over 70μm, much larger than thickness of the SnO_2 layer in film, could be achieved during the Li_2O reversion step.